

# Overcoming contrast reversals in focused probe ptychography of thick materials: an optimal pipeline for efficiently determining local atomic structure in materials science

C. Gao,<sup>1,2</sup> C. Hofer,<sup>1,2</sup> D. Jannis,<sup>1,2</sup> A. Béch e,<sup>1,2</sup> J. Verbeeck,<sup>1,2</sup> and T. J. Pennycook<sup>1,2</sup>

<sup>1</sup>EMAT, University of Antwerp

<sup>2</sup>NANOLab Center of Excellence, University of Antwerp

(\*Electronic mail: timothy.pennycook@uantwerpen.be)

(Dated: 30 May 2022)

Ptychography provides highly efficient imaging in scanning transmission electron microscopy (STEM), but questions have remained over its applicability to strongly scattering samples such as those most commonly seen in materials science. Although contrast reversals can appear in ptychographic phase images as the projected potentials of the sample increase, we show here how these can be easily overcome by a small amount of defocus. The amount of defocus is small enough that it can exist naturally when focusing using the annular dark field (ADF) signal, but can also be adjusted post acquisition. The ptychographic images of strongly scattering materials are clearer at finite doses than other STEM techniques, and can better reveal light atomic columns within heavy lattices. In addition data for ptychography can now be collected simultaneously with the fastest of ADF scans. This combination of sensitivity and interpretability presents an ideal workflow for materials science.

The ability of STEM to determine structure and composition has made it an essential tool in materials science. Typically this has been via Z-contrast ADF imaging<sup>1–3</sup>, with the option of simultaneous spectroscopies providing even greater compositional sensitivity at the cost of far higher doses and drift<sup>4,5</sup>. One particularly prominent deficiency of ADF imaging is the difficulty the modality faces in resolving light atoms near heavy elements. The precise locations of such light elements can dramatically alter the properties of the materials containing them. Such is the case, for example, in many oxides where tiny changes in bond angles or bond lengths can completely change their magnetic or electronic properties<sup>6–8</sup>. Given sufficient stability of the stage and the sample, EELS can reveal the locations of such light elements. However, drift remains a challenge for precise measurements of atomic locations in EELS, and for many materials systems the damage from the doses required for spectroscopy preclude its use at atomic resolution. In many other materials, the propensity to damage under the electron beam also precludes atomic resolution ADF imaging<sup>9</sup>. Alternative means of imaging with both greater sensitivity to light elements and higher overall dose efficiency have thus been sought to complement ADF imaging<sup>10,11</sup>.

Annular bright field (ABF) became popular because it can often determine the locations of light elements in heavy lattices at higher precision and at lower doses than spectroscopic elemental mapping<sup>12–15</sup>. Recently methods based on tracking the center of mass (CoM) of the electron scattering have begun to take over from ABF, as they are able to provide a higher signal to noise ratio. Integrated differential phase contrast (iDPC)<sup>16</sup> and integrated CoM (iCoM)<sup>17,18</sup> have shown particular promise in this regard. iDPC can be performed using a set of conventional detectors arranged into quadrants or segments<sup>16,19</sup>, while iCoM is performed using 4D STEM data from a pixelated camera. Thus while iCoM utilizes a more accurate measure of the CoM, most cameras used for 4D STEM have made it significantly slower than iDPC. Now

however developments in camera technology have made 4D STEM possible without any decrease in scan speed compared to even the most rapid ADF imaging<sup>20</sup>. This technological advance also accelerates the acquisition speed of highly efficient ptychography<sup>21–23</sup>. Direct focused probe forms of ptychography are compatible with simultaneous ADF imaging, but their applicability to stronger objects such as thicker samples containing heavier elements have remained in question due to the use of the weak phase object (WPO) or multiplicative approximations in the theory underlying these ptychographic methods<sup>22,24–27</sup>.

Here we demonstrate the significant advantages of combining focused probe ptychography with conventional rapid scan ADF workflows for the thicker samples typical of materials science. Both the single side band (SSB) and Wigner distribution deconvolution (WDD) methods, both ptychographic methods are capable of providing significantly clearer images of thick structures at lower doses than both ABF and iCoM. This is true well beyond the approximations used in the theoretical description of the methods. Although complex thickness induced contrast reversals can appear in the SSB and WDD phase images, as has previously been shown<sup>26</sup>, we show how small amounts of defocus can remove these effects and provide contrast reversal free images that can clearly show the positions of all the atomic columns in thick structures. These small amounts of defocus are often within the range of defocus that is set naturally when optimizing ADF images manually in conventional imaging, but can also be applied and optimized after acquiring the data due to the ability of ptychography to perform post collection aberration correction.

In both SSB and WDD ptychography the relative phases of diffracted convergent beam electron diffraction (CBED) disks are solved via their mutual interference with the direct beam in probe position reciprocal space. Experiments proceed by recording the intensity distribution of the bright field disk as a function of probe position with a camera. The Fourier trans-

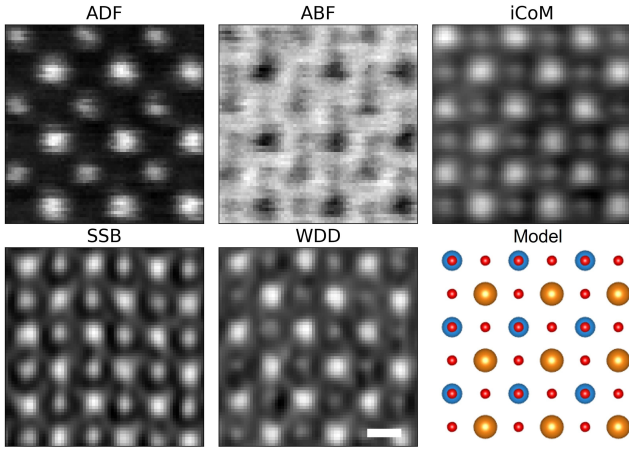


FIG. 1. ADF and Medipix3 based 4D STEM data from  $\text{SrTiO}_3$ . iCoM and ptychography show the O columns more clearly than the ABF. However this data shows some drift from the slow scan imposed by the camera. Sr, Ti and O columns are indicated by orange, blue and red respectively in the overlays. Scale bar: 2 Ångstroms.

form of this 4D STEM data with respect to probe position yields, in the multiplicative approximation<sup>25</sup>,

$$G(\mathbf{K}_f, \mathbf{Q}_p) = A(\mathbf{K}_f)A^*(\mathbf{K}_f + \mathbf{Q}_p) \otimes_{\mathbf{K}_f} \Psi_s(\mathbf{K}_f)\Psi_s^*(\mathbf{K}_f - \mathbf{Q}_p), \quad (1)$$

in which  $\mathbf{K}_f$  is the scattering vector leading to a location on the camera,  $\mathbf{Q}_p$  is spatial frequency,  $A$  is an aperture function expressing both the effect of the aperture size and the aberrations that appear within it, and  $\Psi_s$  represents the Fourier transform of the specimen transmission function. This represents the convolution between the region of mutual overlap of the shifted and unshifted aperture functions and the interference of the diffracted beams differing in frequency by  $\mathbf{Q}_p$ . In SSB ptychography the WPO approximation is invoked to further simplify this to<sup>21</sup>

$$G(\mathbf{K}_f, \mathbf{Q}_p) = |A(\mathbf{K}_f)|^2 \delta(\mathbf{Q}_p) + A(\mathbf{K}_f)A^*(\mathbf{K}_f + \mathbf{Q}_p)\Psi_s^*(-\mathbf{Q}_p) + A^*(\mathbf{K}_f)A(\mathbf{K}_f - \mathbf{Q}_p)\Psi_s(\mathbf{Q}_p), \quad (2)$$

from which it can be understood how to straightforwardly obtain the phase and amplitude of each frequency of the specimen transmission function from the double disk overlap regions where the shifted and unshifted aperture functions coincide<sup>22</sup>. In WDD the WPO approximation is avoided and deconvolution is used to separate the aperture functions from the specimen transmission function<sup>25</sup>. However the principle remains essentially the same in that the phase and amplitude of each spatial frequency relative to the direct beam is determined from the double overlap regions.

Although the details of CBED patterns are highly dependent on thickness, both the WDD and SSB can in practice be seen to provide clear images of the structures of materials containing heavy elements that are tens of nanometers thick from both experiments and simulations. An experimental example using a Medipix3 camera is shown with  $\text{SrTiO}_3$  in figure

1 comparing simultaneous ADF and 4D STEM based ABF, iCoM and the focused probe SSB and WDD ptychography signals. The conditions were optimized for the ADF image during the acquisition at 200 kV with a 20 mrad convergence angle. Distortions due to drift are apparent due to the very slow speed of the scan compared to conventional ADF imaging. The 2400 frames per second speed of the 6 bit mode of the Medipix3 camera used here is a relatively typical speed for 4D STEM cameras over the past five years. However it is clear that both SSB and WDD provide atomic resolution images that, along with the iCoM, are far clearer than that of the ABF, despite the strength of the scattering here. A degree of filtering is apparent, but most of the clarity is attributed to the dose efficiency of the iCoM and ptychographic methods. The thickness is most likely on the order of tens of nanometers from the position averaged CBED data (see supplementary information) which puts this sample well beyond both the WPO and multiplicative approximations. Note that the ADF remains useful for clearly distinguishing the Sr and Ti columns, but the O atoms are not visible without the additional signals.

Although frame based direct detection 4D STEM cameras such as the Medipix3 and its competitors are faster and more efficient than previous generation cameras, and are continuing to improve, the drift resulting from their still relatively low speeds remains a major problem for precision measurements. Furthermore the slow scan speeds they impose also make it more difficult to reach low doses. These two issues, drift and dose, have thus motivated continued use of methods based instead on conventional STEM detector setups such as ABF and iDPC which are in many ways inferior to 4D STEM methods but which have so far been more practical<sup>17,22,24,28</sup>.

Now however we can remove the camera as a bottleneck to the speed at which 4D STEM can be performed. With event based detectors such as the Timepix3<sup>20</sup>, we can easily reach the equivalent of not just a few thousand frames per second as in the example shown in Figure 1, but millions of frames per second. We refer to frames per second equivalent here in relation to the event driven camera only for the ease of comparison it can provide, as event driven operation does not utilize camera frames. Instead, each electron detected by the camera is labeled with a pixel location and time, and readout directly after the hit occurs rather than waiting for a full camera frame to be exposed and read out together. This provides a more efficient readout that enables us to easily perform 4D STEM at the single to few microsecond dwell times used in rapid scan ADF imaging. Faster scans are also possible, such as the 100 ns dwell time we demonstrated previously<sup>20</sup>, and may become increasingly desirable with the enhanced dose efficiency available with CoM and especially ptychography, assuming the scan system can keep up. Indeed we can also perform the same type of drift corrected multiple scan based imaging as has become common in rapid scan ADF imaging, allowing us to use data up until the point damage sets in. Thus with event driven cameras 4D STEM can now be acquired as rapidly as any other STEM modality.

We illustrate the step change in the quality of images this provides in Figure 2 with 4D STEM data acquired on a

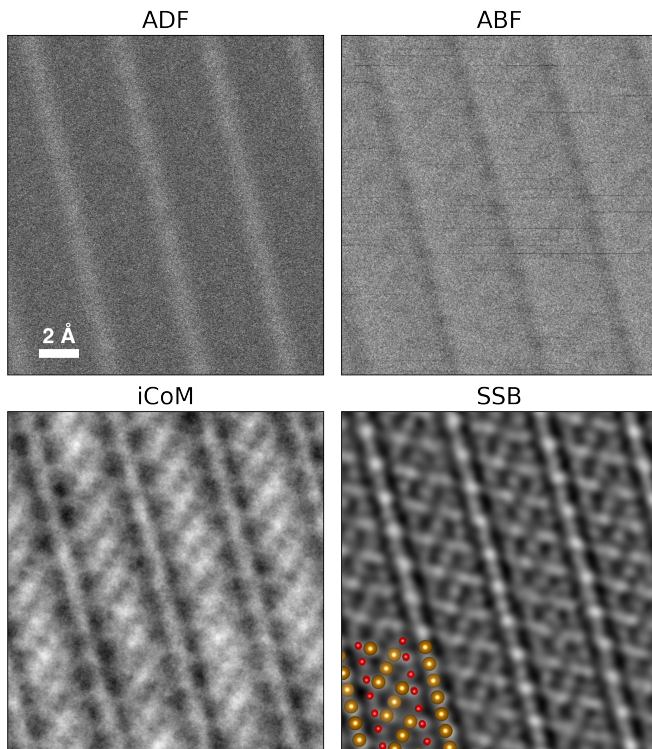


FIG. 2. ADF, ABF, iCoM and SSB images of  $\text{Fe}_3\text{O}_4$  reconstructed from the same 4D dataset captured with a Timepix3. Despite the low dose, the SSB image clearly shows the oxygen columns. The crystallinity and absence of distortions allowed the full image to be divided into 4 parts and aligned, based on the SSB signal, and averaged to produce the higher signal-to-noise ratio images shown. O and Fe atoms are shown in red and brown respectively in the model.

Timepix3 complementing ADF data collected simultaneously from  $\text{Fe}_3\text{O}_4$ , again using 200kV and a 20 mrad convergence angle. The electron dose is  $10000 e^-/\text{\AA}^2$ . The dwell time of the probe is 2 microseconds. The ADF signal was used to optimize the imaging conditions, just as in a standard high end ADF STEM workflow. As seen in Figure 1 the clarity of the iCoM and focused probe ptychography far exceed that of the ABF image. However unlike Figure 1, this scan is essentially drift free and at much lower dose. Because of the relatively low dose employed, the ADF is extremely noisy, as is the ABF signal which provides very little obvious advantage over the ADF signal for locating the atoms in the structure. With the lower dose used here, the strength of the focused probe ptychography over that of iCoM also becomes more apparent. Essentially every single atomic column is visible in the focused probe ptychography, but they are not in the iCoM.

Although the contrast transfer functions of both SSB and WDD ptychography are single signed and provide easily interpretable images in which the contrast of the atoms is consistent against the background for thin weak specimens<sup>24,29</sup>, the contrast becomes more complex when handling thicker samples. Complex changes in contrast can appear as the projected potential of the sample becomes stronger as evidenced previously in  $\text{GaN}$ <sup>26</sup>. Atomic columns can be seen to change from

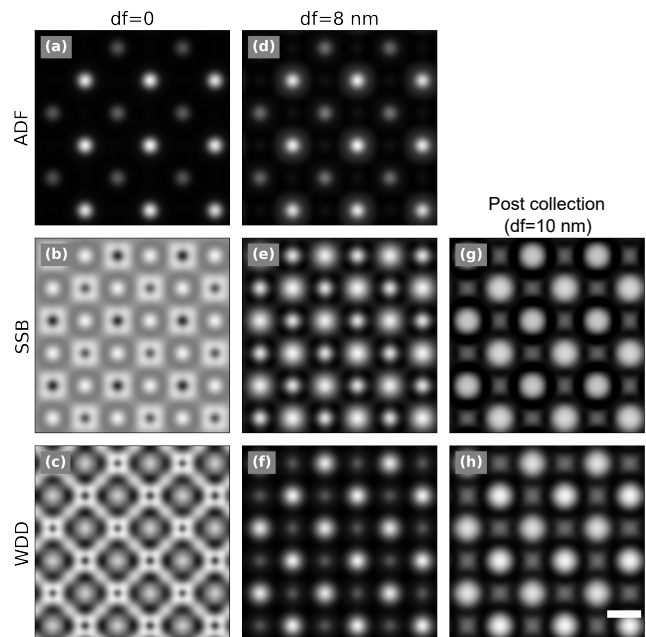


FIG. 3. ADF, SSB and WDD ptychographic images reconstructed from the simulated 4D datasets (20 nm thickness [100] STO) with different defocus values. Figure 3. (a), (b) and (c) are the ADF, SSB and WDD ptychographic images reconstructed from the simulated dataset with defocus value 0. Figure 3. (d), (e) and (f) are the ADF, SSB and WDD ptychographic images reconstructed from the simulated 4D dataset with defocus value 8 nm. Figure 3.(g) and (h) are the SSB and WDD ptychographic images with post collection from the dataset in figure 3.(a), (b) and (c). Scale bar: 2 Ångstroms.

bright to dark as the sample thickens, generally beginning in the center of the atomic columns where the projected potential is strongest. Thus one can encounter images in which the center of atomic columns have become dark while further out they remain bright. Such complex contrast reversals can not only impede the ease of interpretability but also degrade the dose efficiency by reducing the available contrast in low dose images.

An example of these contrast reversals in phase is shown with simulations in Figure 3 (b) and (c). The voltage and convergence angle are the same as those used for the experimental data shown in Figure 1. With the probe focused to the entrance surface of the 20 nm thick [100] oriented STO (zero defocus), both the SSB and WDD produce complex phase images in which the centers of both the Ti and Sr columns are dark but the light O columns remain bright. Surrounding the dark centers of the Ti and Sr columns are regions of higher phase values before these reduce to an intermediate phase value in the background. It is still possible to interpret which columns are where, particularly with the ADF signal present and indeed, the O columns already appear bright. However, these complex contrast reversals are clearly often undesirable, and by applying a small amount of defocus it is possible to remove them. This is illustrated in Figure 3 for SSB (e) and WDD (f) with a defocus of 8 nm which has a minimal affect on the contrast of the ADF image. With this defocus all the atomic

columns appear bright on a dark background in the ptychographic images.

In Figure 3 we additionally show the effect of adding 10 nm of defocus aberration post collection to 4D STEM data simulated at zero defocus with the SSB (g) and WDD (h). 10 nm was chosen as it optimizes the removal of the contrast reversals. Although not identical to performing the defocus adjustment on the probe directly, this illustrates that post acquisition adjustment can indeed be used to remove the contrast reversals. This difference between applying the defocus during and after acquisition could be explained by channeling effects which are not accounted for with the post acquisition adjustment of the defocus.

The availability of the simultaneous ADF signal is thus of two fold importance. Its atomic number contrast provides greater compositional discernment without resorting to the greater doses required for atomic resolution spectrum imaging, while providing a reference image which is not susceptible to contrast reversals. Atoms are always bright on a dark background in ADF images. This advantage is not available in defocused probe methods of ptychography because the ADF image is blurred beyond usability. Furthermore the direct forms of ptychography require no iterative solution and can thus be available very quickly after collection.

Although elucidating the physics of the removal of contrast reversals via defocus in detail is reserved for future studies, we believe the effect can be understood as rolling the phase around across the field of view such that the centers of the atomic columns are maximum and the background at a minimum. This works in practice because the ptychographic phase images generally only use a small fraction of the  $2\pi$  radian range of values available for phase value images, and thus the phase rolling does not bring other features into non intuitive ranges of contrast.

In both of our experimental examples, the ptychographic data did not require additional defocus to produce clear images. This could be because they happened to be obtained at a focus that produced both clear ADF and ptychographic images. As seen in figure 3, the defocus applied there to provide contrast reversal free ptychographic images only slightly reduced the quality of the ADF image. However in cases where the defocus is not optimal for the ptychography, it can be adjusted after taking the ptychographic data. The injection of defocus and post collection aberration correction generally has been demonstrated previously<sup>25,29</sup> with focused probe ptychography, but here provides an unanticipated extra benefit in addition to removing lens aberrations or indeed performing optical sectioning post collection. Post collection aberration correction can of course also be combined with a defocus optimization to also remove undesirable residual aberrations that remain in even the most advanced aberration corrected instruments today.

In comparison to iterative ptychographic techniques, the direct methods offer the advantage of not only removing the question of convergence but enhanced processing speed. Iterative techniques are not guaranteed to converge, or indeed to converge to the correct result, especially at lower doses, but they are guaranteed to take a longer time to produce a use-

ful image. For comparison, we timed serial SSB and ePIE calculations from the same 47 by 47 probe position focused probe 4D dataset simulated free of aberrations for single unit cell thick STO performed on an i7-10700K processor. The entire SSB calculation takes 2.4 s regardless of dose. The full field ePIE results took 24.4 s per iteration and an ePIE calculation restricted to just the BF disk took 3.47 s per iteration, with the final results dependent on the dose and the number of iterations. Even at infinite dose the BF disk only ePIE was significantly less clear than the SSB with the O columns at least difficult to discern after even 100 iterations (346 s). The higher resolution of the full field ePIE produces sharper images than the SSB when reasonable convergence is achieved. At  $1.2 \times 10^5 e^-/\text{\AA}^2$  the ePIE algorithm does not converge. At  $1.5 \times 10^5 e^-/\text{\AA}^2$  and above the full field ePIE converges to a useful image within 10 to 40 iterations depending on the desired convergence level. With 10 iterations taking 244 s the full field ePIE takes about 100 times longer than the SSB, and the SSB additionally has no issue producing clear images when the ePIE fails to converge. For further details see the Supplementary Information.

While significant parallelism can be employed to speed up these times, these results reflect the much greater computational time needed for iterative solutions and the fact they can fail to converge at low doses in a way that is particularly problematic for the focused probe configuration desired for ADF imaging. Thus although some additional post processing time for an optimised ptychographic image using the best defocus adjustment or additional post collection aberration correction might be desirable, direct ptychography methods can produce useful output very quickly after acquiring the data. How fast constitutes live imaging can be debated, but live iCoM<sup>30</sup> and SSB<sup>31</sup> have been reported already, and further speed improvements are anticipated from further optimization, including both better parallelization and greater leveraging of the sparse nature of the data produced by event driven cameras.

In conclusion, we have demonstrated the utility of performing focused probe ptychography within existing rapid scan ADF workflows for general materials science samples. Simultaneous ADF and ptychography provide a robust and interpretable method of efficiently imaging all the atomic columns in such samples. In particular, when combined with the ability to apply corrective defocus, the method works well beyond the approximations which have been used to motivate the SSB and WDD methods. The clarity of the ptychographic images, provides the best possible combination of the general efficiency of structural imaging, visibility of light elements and interpretability when combined with simultaneous Z-contrast ADF imaging. With a detector such as the Timepix3, drift is no longer a significant issue with 4D STEM and there is indeed very little reason not to perform simultaneous ADF and 4D STEM imaging. We therefore anticipate the widespread adoption of this imaging pipeline in the future.

## ACKNOWLEDGEMENTS

We acknowledge funding from the European Research Council (ERC) under the European Union's Horizon 2020 research and innovation programme (C.G., C.H. and T.J.P.) via 802123-HDEM. This project has received funding from the European Union's Horizon 2020 Research Infrastructure - Integrating Activities for Advanced Communities under grant agreement No 823717 – ESTEEM3. J.V. and D.J. acknowledge funding from FWO project, Belgium G042920N "Coincident event detection for advanced spectroscopy in transmission electron microscopy" and J.V. and A. B. acknowledge funding from G042820N "Exploring adaptive optics in transmission electron microscopy". We acknowledge funding under the European Union's Horizon 2020 research and innovation programme (J.V. and D.J.) under grant agreement No 101017720 "eBEAM: Electron beams enhancing analytical microscopy".

- <sup>1</sup>S. J. Pennycook, "Z-contrast STEM for materials science," *Ultramicroscopy* **30**, 58–69 (1989).
- <sup>2</sup>S. J. Pennycook and D. Jesson, "High-resolution Z-contrast imaging of crystals," *Ultramicroscopy* **37**, 14–38 (1991).
- <sup>3</sup>O. L. Krivanek, M. F. Chisholm, V. Nicolosi, T. J. Pennycook, G. J. Corbin, N. Dellby, M. F. Murfitt, C. S. Own, Z. S. Szilagy, M. P. Oxley, S. T. Pantelides, and S. J. Pennycook, "Atom-by-atom structural and chemical analysis by annular dark-field electron microscopy," *Nature* **464**, 571–574 (2010).
- <sup>4</sup>P. Perna, D. Maccariello, M. Radovic, U. S. di Uccio, I. Pallecchi, M. Codda, D. Marre, C. Cantoni, J. Gazquez, M. Varela, S. J. Pennycook, and F. M. Granozio, "Conducting interfaces between band insulating oxides: The LaGaO<sub>3</sub>/SrTiO<sub>3</sub> heterostructure," *Applied physics letters* **97** (2010).
- <sup>5</sup>W. Zhou, M. D. Kapetanakis, M. P. Prange, S. T. Pantelides, S. J. Pennycook, and J.-C. Idrobo, "Direct determination of the chemical bonding of individual impurities in graphene," *Phys. Rev. Lett.* **109**, 206803 (2012).
- <sup>6</sup>C. Ge, K.-J. Jin, Q.-H. Zhang, J.-Y. Du, L. Gu, H.-Z. Guo, J.-T. Yang, J.-X. Gu, M. He, J. Xing, C. Wang, H.-B. Lu, and G.-Z. Yang, "Toward switchable photovoltaic effect via tailoring mobile oxygen vacancies in perovskite oxide films," *ACS applied materials & Interfaces* **8**, 34590–34597 (2016).
- <sup>7</sup>G. Ou, Y. Xu, B. Wen, R. Lin, B. Ge, Y. Tang, Y. Liang, C. Yang, K. Huang, D. Zu, R. Yu, W. Chen, J. Li, H. Wu, L.-M. Liu, and Y. Li, "Tuning defects in oxides at room temperature by lithium reduction," *Nature communications* **9** (2018).
- <sup>8</sup>M. Wu, S. Chen, and W. Xiang, "Oxygen vacancy induced performance enhancement of toluene catalytic oxidation using LaFeO<sub>3</sub> perovskite oxides," *Chemical engineer journal* **387** (2020).
- <sup>9</sup>R. Egerton, "Radiation damage and nanofabrication in TEM and STEM," *Microscopy Today* **29**, 56–59 (2021).
- <sup>10</sup>K. C. Bustillo, S. E. Zeltmann, M. Chen, J. Donohue, J. Ciston, C. Ophus, and A. M. Minor, "4D-STEM of beam-sensitive materials," *Accounts of chemical research* **54**, 2543–2551 (2021).
- <sup>11</sup>A. Velazco, A. Béché, D. Jannis, and J. Verbeeck, "Reducing electron beam damage through alternative STEM scanning strategies, Part I: Experimental findings," *Ultramicroscopy* **232**, 113398 (2022).
- <sup>12</sup>S. D. Findlay, N. Shibata, H. Sawada, E. Okunishi, Y. Kondo, T. Yamamoto, and Y. Ikuhara, "Robust atomic resolution imaging of light elements using scanning transmission electron microscopy," *Applied physics letters* **95** (2009).
- <sup>13</sup>R. Ishikawa, E. Okunishi, H. Sawada, Y. Kondo, F. Hosokawa, and E. Abe, "Direct imaging of hydrogen-atom columns in a crystal by annular bright-field electron microscopy," *Nature materials* **10**, 278–281 (2011).
- <sup>14</sup>S. D. Findlay, N. Shibata, H. Sawada, E. Okunishi, Y. Kondo, and Y. Ikuhara, "Dynamics of annular bright field imaging in scanning transmission electron microscopy," *Ultramicroscopy* **110**, 903–923 (2010).
- <sup>15</sup>Y.-M. Kim, S. J. Pennycook, and A. Y. Borisevich, "Quantitative comparison of bright field and annular bright field imaging modes for characterization of oxygen octahedral tilts," *Ultramicroscopy* **181**, 1–7 (2017).
- <sup>16</sup>E. Yucelen, I. Lazic, and E. G. T. Bosch, "Phase contrast scanning transmission electron microscopy imaging of light and heavy atoms at the limit of contrast and resolution," *Scientific reports* **8**, 2676 (2018).
- <sup>17</sup>I. Lazic, E. G. Bosch, and S. Lazar, "Phase contrast STEM for thin samples: Integrated differential phase contrast," *Ultramicroscopy* **160**, 265–280 (2016).
- <sup>18</sup>J. A. Hachtel, J. C. Idrobo, and M. Chi, "Sub-Angstrom electric field measurements on a universal detector in a scanning transmission electron microscope," *Advanced structural and chemical imaging* **4**, 10 (2018).
- <sup>19</sup>Z. Li, J. Biskupek, U. Kaiser, and H. Rose, "Integrated differential phase contrast (IDPC)-STEM utilizing a multi-sector detector for imaging thick samples," *Microscopy and Microanalysis*, 1–11 (2022).
- <sup>20</sup>D. Jannis, C. Hofer, C. Gao, X. Xie, A. Béché, T. Pennycook, and J. Verbeeck, "Event driven 4D STEM acquisition with a Timepix3 detector: Microsecond dwell time and faster scans for high precision and low dose applications," *Ultramicroscopy* **233**, 113423 (2022).
- <sup>21</sup>J. Rodenburg, B. McCallum, and P. Nellist, "Experimental tests on double-resolution coherent imaging via STEM," *Ultramicroscopy* **48**, 304–314 (1993).
- <sup>22</sup>T. J. Pennycook, A. R. Lupini, H. Yang, M. F. Murfitt, L. Jones, and P. D. Nellist, "Efficient phase contrast imaging in stem using a pixelated detector. Part I: Experimental demonstration at atomic resolution," *Ultramicroscopy* **151**, 160–167 (2015).
- <sup>23</sup>Y. Jiang, Z. Chen, Y. Hang, P. Deb, H. Gao, S. Xie, P. Purohit, M. W. Tate, J. Park, S. M. Gruner, V. Elser, and D. A. Muller, "Electron ptychography of 2D materials to deep sub-Angstrom resolution," *Nature* **559**, 343–349 (2018).
- <sup>24</sup>H. Yang, T. J. Pennycook, and P. D. Nellist, "Efficient phase contrast imaging in stem using a pixelated detector. Part II: Optimisation of imaging conditions," *Ultramicroscopy* **151**, 232–239 (2015).
- <sup>25</sup>H. Yang, R. N. Rutte, L. Jones, M. Simson, R. Sagawa, H. Ryll, M. Huth, T. J. Pennycook, M. L. H. Green, H. Soltau, Y. Kondo, B. G. Davis, and P. D. Nellist, "Simultaneous atomic-resolution electron ptychography and Z-contrast imaging of light and heavy elements in complex nanostructures," *Nature communications* **7** (2016).
- <sup>26</sup>H. Yang, I. MacLaren, L. Jones, G. T. Martinez, M. Simson, M. Huth, H. Ryll, H. Soltau, R. Sagawa, Y. Kondo, C. Ophus, P. Ercius, L. Jin, A. Kovács, and P. D. Nellist, "Electron ptychographic phase imaging of light elements in crystalline materials using wigner distribution deconvolution," *Ultramicroscopy* **180**, 173–179 (2017).
- <sup>27</sup>T. J. Pennycook, G. T. Martinez, P. D. Nellist, and J. C. Meyer, "High dose efficiency atomic resolution imaging via electron ptychography," *Ultramicroscopy* **196**, 131–135 (2019).
- <sup>28</sup>K. Mueller, F. F. Krause, A. Beche, M. Schowalter, V. Galioit, S. Loeffler, J. Verbeeck, J. Zweck, P. Schattschneider, and A. Rosenauer, "Atomic electric fields revealed by a quantum mechanical approach to electron ptychography," *Nature communication* **5**, 5653 (2014).
- <sup>29</sup>C. M. O'Leary, G. T. Martinez, E. Liberti, M. J. Humphry, A. I. Kirkland, and P. D. Nellist, "Contrast transfer and noise considerations in focused-probe electron ptychography," *Ultramicroscopy* **221**, 113189 (2021).
- <sup>30</sup>C.-P. Yu, T. Friedrich, D. Jannis, S. Van Aert, and J. Verbeeck, "Real time integration centre of mass (riCOM) reconstruction for 4D-STEM," (2021), arXiv:2112.04442.
- <sup>31</sup>A. Strauch, D. Weber, A. Clausen, A. Lesnichaia, A. Bangun, B. März, F. J. Lyu, Q. Chen, A. Rosenauer, R. Dunin-Borkowski, and et al., "Live processing of momentum-resolved STEM data for first moment imaging and ptychography," *Microscopy and Microanalysis* **27**, 1078–1092 (2021).

**Supplementary Information:**

**Overcoming contrast reversals in focused probe ptychography of thick materials:  
an optimal pipeline for efficiently determining local atomic structure in materials  
science**

C. Gao,<sup>1,2</sup> C. Hofer,<sup>1,2</sup> D. Jannis,<sup>1,2</sup> J. Verbeeck,<sup>1,2</sup> and T. J. Pennycook<sup>1,2</sup>

<sup>1</sup>*EMAT, University of Antwerp*

<sup>2</sup>*NANOLab Center of Excellence, University of Antwerp*

(\*Electronic mail: [timothy.pennycook@uantwerpen.be](mailto:timothy.pennycook@uantwerpen.be))

(Dated: 30 May 2022)

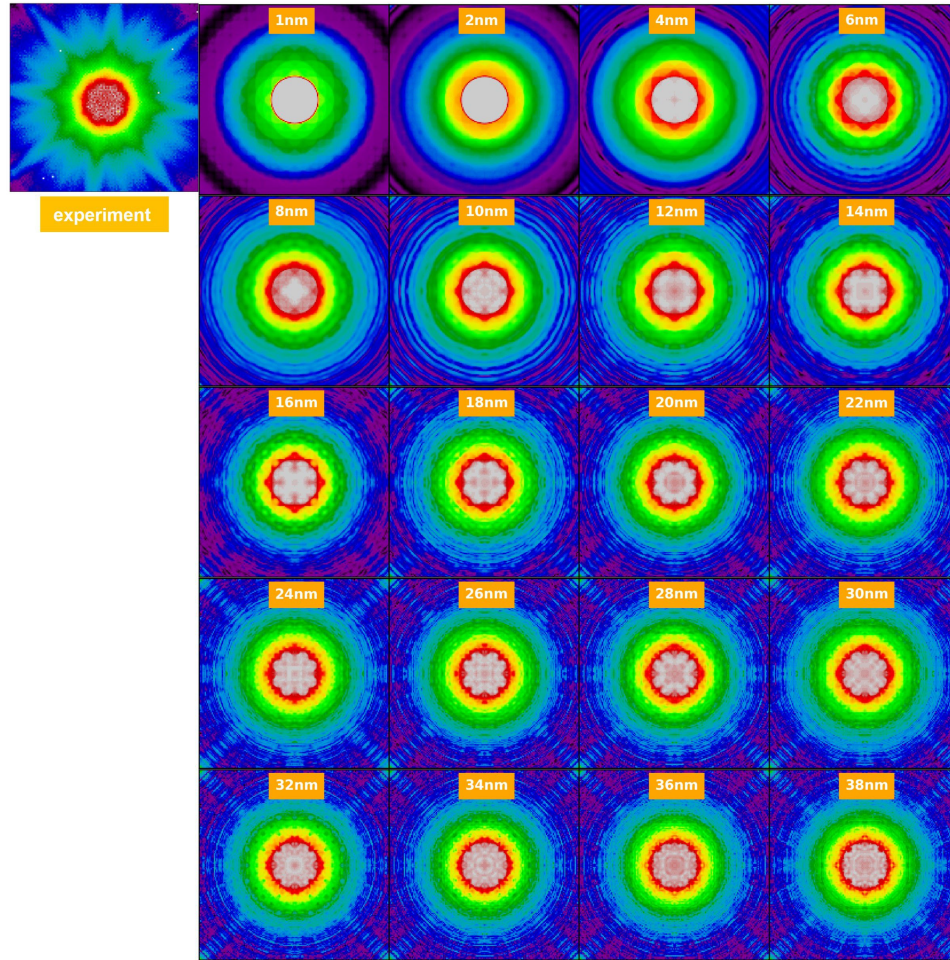


FIG. 1. Comparison of the PACBED from the experimental data used for Figure 1 of the main text with PACBED simulated for different STO sample thicknesses using the same 200 kV accelerating voltage and 20 mrad convergence angle used in the experiment. While no single thickness provides a perfect match, it is clear the experimental PACBED is consistent with the sample tens of nanometers thick. Looking at the symmetries present, we estimate the experiment was performed in a region that is a least approximately 20 nm thick. Scale bar is 2 Ångstroms.

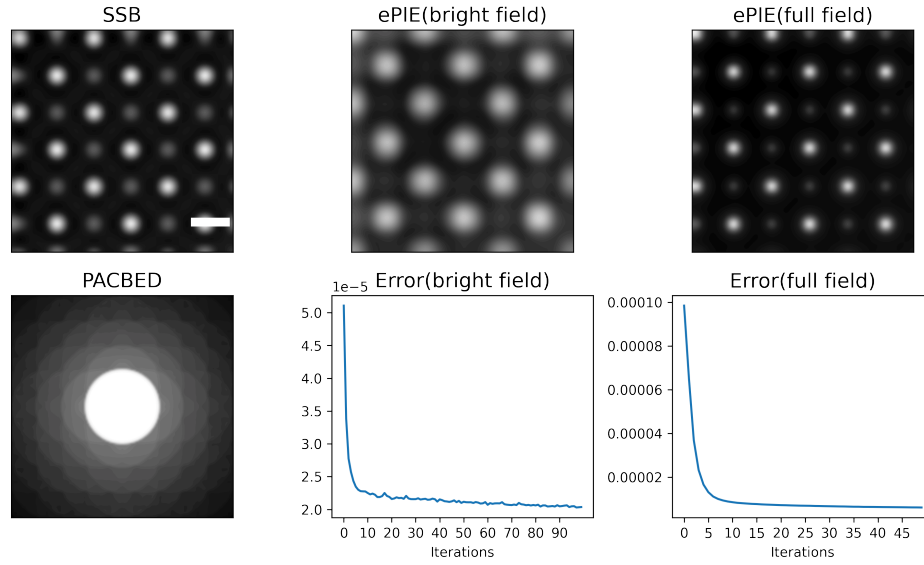


FIG. 2. ePIE and SSB results computed using a single core of an i7-10700K operating at 3.8 GHz using data simulated for a single unit cell of STO at 200 KV, with a 20 mrad convergence angle and zero defocus and a 59 by 59 probe position grid. The 47 by 47 pixels of the bright field disk are used for bright field ePIE, while 137 by 137 pixels of the full field CBED patterns are used for full field ePIE. The SSB image was computed in a total time of 2.4 s. 100 iterations was used in computing the bright field ePIE result taking a total time of 347 s, for an average of 3.47 seconds per iteration. The full field ePIE result and the error for per iteration are also provided. The PACBED of the STO dataset is also shown with a log scale.

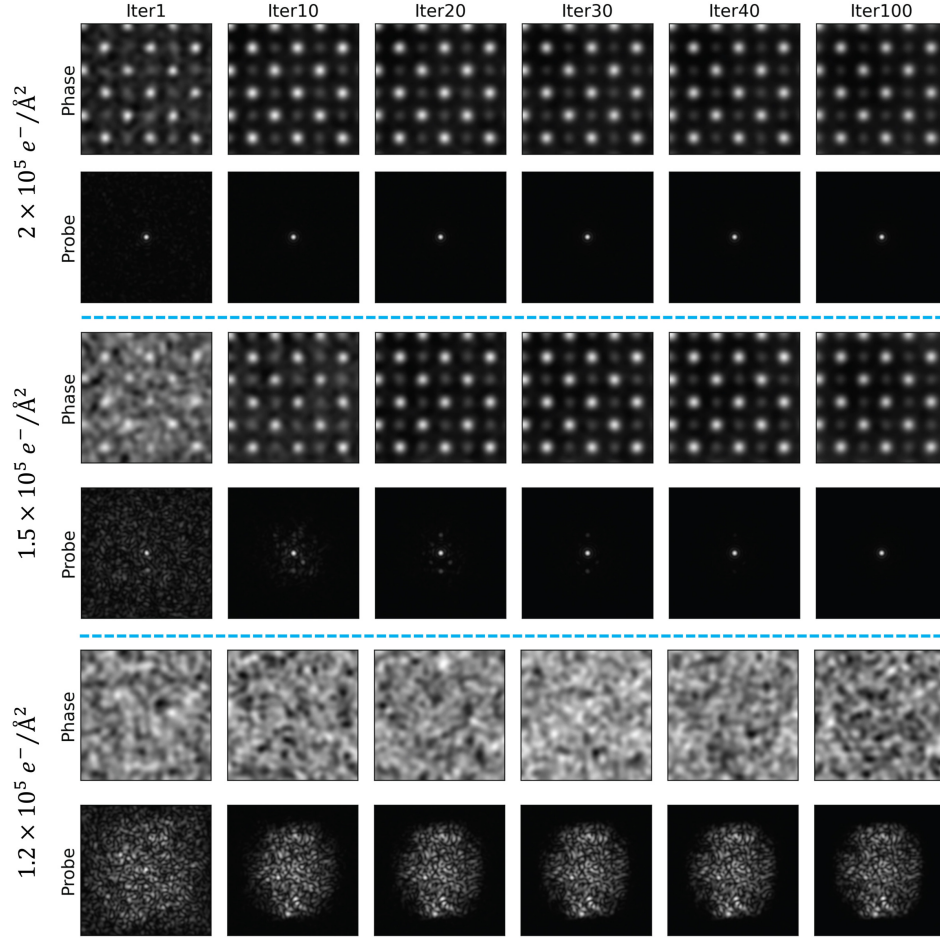


FIG. 3. Full field single unit cell thick STO ePIE reconstruction as a function of iteration number at different doses. At  $2 \times 10^5 e^-/\text{\AA}^2$ , after 10 to 20 iterations very little apparent change occurs in the phase and probe. At  $1.5 \times 10^5 e^-/\text{\AA}^2$  some artefacts are visible at 20 iterations, but disappear between iterations 30 to 40. At  $1.2 \times 10^5 e^-/\text{\AA}^2$  the algorithm does not converge even after 100 iterations, reflecting the fact that the convergence of ePIE depends critically on the amount of signal in the CBED patterns. We note that using a significantly defocused probe increases the signal per CBED pattern, but a strongly defocused probe precludes useful simultaneous Z-contrast ADF imaging.

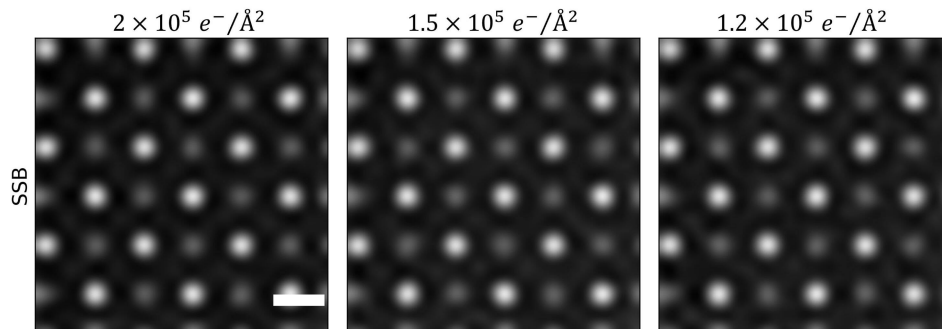


FIG. 4. SSB reconstructions at the same doses as shown in SI Figure 3. As a direct non-iterative method, SSB ptychography does not depend on the dose to converge. Of course, the clarity of the resulting SSB images do depend on the dose, but it is a consistent and immediate result, and the above doses pose no problem at all for the SSB method. Scale bar is 2 Ångstroms.